

Tissue fluidity promotes epithelial wound healing

Robert J. Tetley^{1,2}, Michael F. Staddon^{2,3}, Davide Heller^{4,5}, Andreas Hoppe⁶, Shiladitya Banerjee^{2,3} and Yanlan Mao^{1,2,7*}

The collective behaviour of cells in epithelial tissues is dependent on their mechanical properties. However, the contribution of tissue mechanics to wound healing in vivo remains poorly understood. Here, we investigate the relationship between tissue mechanics and wound healing in live *Drosophila* wing imaginal discs and show that by tuning epithelial cell junctional tension, we can systematically alter the rate of wound healing. Coincident with the contraction of an actomyosin purse string, we observe cells flowing past each other at the wound edge by intercalating, reminiscent of molecules in a fluid, resulting in seamless wound closure. Using a cell-based physical model, we predict that a reduction in junctional tension fluidizes the tissue through an increase in intercalation rate and corresponding reduction in bulk viscosity, in the manner of an unjamming transition. The resultant fluidization of the tissue accelerates wound healing. Accordingly, when we experimentally reduce tissue tension in wing discs, the intercalation rate increases and wounds repair in less time.

Epithelial tissues are inevitably damaged from time to time and must therefore have robust repair mechanisms. The behaviour of cells and tissues, for example during wound healing and morphogenesis, depends on their mechanical properties and those of the surrounding environment¹. Previous studies have investigated the contribution of tissue mechanics to epithelial wound healing primarily using in vitro cell culture assays^{2–7}. However, whether these in vitro assays truly recapitulate the physiological response of in vivo tissues is unclear. Many in vivo models of epithelial wound healing have been developed⁷, although the mechanical basis of the wound healing process in such in vivo systems remains unclear. A number of in vivo epithelia have been shown experimentally to form contractile supracellular actomyosin cables^{8–12} at the margin of epithelial wounds, which contract in a purse-string manner and bring the edges of the wound into apposition. Although the mechanical role of the actomyosin purse string has begun to be investigated in vivo^{13,14}, the contribution of surrounding tissue mechanical properties to wound healing remains unclear.

To investigate the role of tissue mechanics in wound healing in an in vivo system, we studied tissue repair in the epithelium of *Drosophila* wing imaginal discs by live time-lapse imaging. After wounding wing discs by laser ablation, an actomyosin purse string assembles at the wound's leading edge (Fig. 1a and Supplementary Video 1), as in other systems^{10,15–18}. To understand the mechanisms controlling repair dynamics, we quantitatively analysed¹⁹ wound morphology over the time course of wound closure. We observe three distinct phases after wounding: recoil, fast closure and slow closure (Fig. 1b and Supplementary Video 2). Immediately after wounding, the wound area increases, due to a release of tissue tension by the ablation. The wound area then reduces in time, with an initial fast phase. However, after reaching ~50% of the original wound area, the rate of wound closure decreases dramatically, until closure. Myosin II (MyoII) intensity increases after wounding, before peaking at roughly twice the initial intensity (Fig. 1c). This peak coincides with the transition between fast and slow closure phases.

The dramatic reduction in wound closure rate at later stages suggested that different cell behaviours may be responsible for the fast and slow phases. By closely examining cell behaviours around the wound, we observe that cells at the wound edge readily undergo intercalation, particularly during the slow closure phase (Fig. 1d,e,g and Supplementary Video 2). This cell behaviour differs from those associated with wound healing in other *Drosophila* tissues (for example, cell fusion^{20,21}, polyploidization²¹ and cell intercalation further from the wound edge²²). We also saw no evidence of protrusion-based active migration or cell extrusion. During wound edge intercalations, junctions in contact with the wound shrink to a single vertex and new junctions grow in the orthogonal direction (Fig. 1d). As a result, the number of cells in contact with the wound decreases over time (Fig. 1e and Supplementary Fig. 1a–d). These wound edge intercalations (involving three cells) are distinct from T1 transitions observed in many systems²³, as a T1 transition involves the rearrangements of four neighbouring cells (Supplementary Methods). The rate at which wound edge cells intercalate is roughly 11 times that of unwounded tissue (Fig. 1f) and there is a strong relationship between wound edge intercalation and the reduction in wound area during the slow phase of wound closure (Fig. 1g), indicating that wound edge cell intercalation might be required to promote the completion of wound closure.

To quantitatively test the role of wound edge cell intercalation, we developed a computational vertex model²⁴ for wound closure in the wing disc (Supplementary Fig. 2 and Supplementary Methods). Although the mechanics of wound healing has been modelled previously using continuum^{2,4,6} or finite element approaches^{5,25}, more representative cell-based models, such as vertex models^{26,27}, have rarely been applied to replicate in vivo wound healing dynamics. We model each cell in the tissue as a two-dimensional polygon carrying variable tension on the edges, with bulk elasticity and peripheral contractility (Supplementary Fig. 2a,b and Supplementary Methods). We parameterized the model so that edges contacting the wound gradually increase in tension compared to the surrounding tissue, to mimic the assembly of the contractile actomyosin

¹MRC Laboratory for Molecular Cell Biology, University College London, London, UK. ²Institute for the Physics of Living Systems, University College London, London, UK. ³Department of Physics & Astronomy, University College London, London, UK. ⁴Institute of Molecular Life Sciences, University of Zurich, Zurich, Switzerland. ⁵SIB Swiss Institute of Bioinformatics, Quartier Sorge, Batiment Genopode, Lausanne, Switzerland. ⁶Faculty of Science, Engineering and Computing, Kingston University, Kingston-upon-Thames, UK. ⁷College of Information and Control, Nanjing University of Information Science and Technology, Nanjing, Jiangsu, China. *e-mail: y.mao@ucl.ac.uk

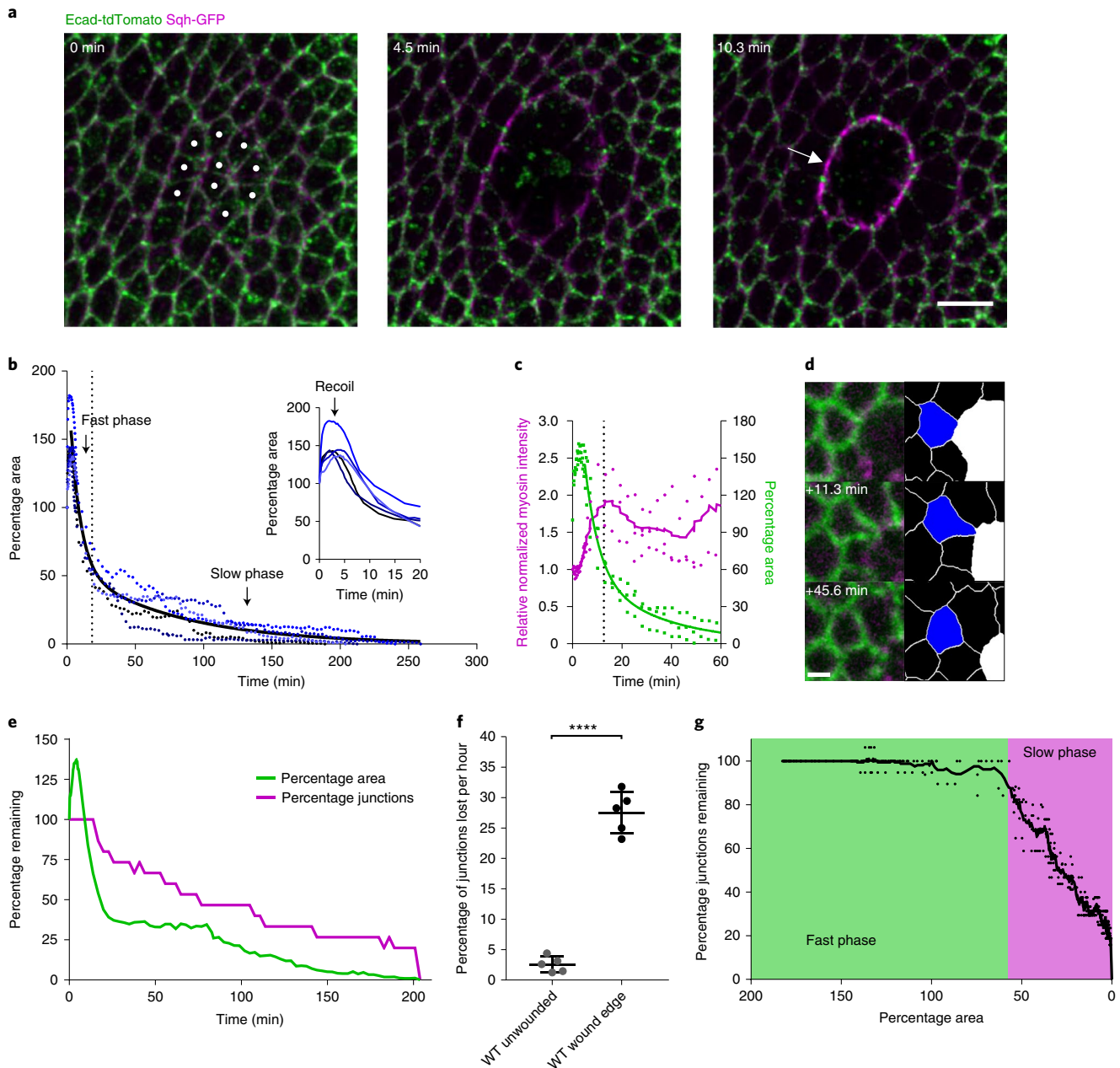


Fig. 1 | Wing disc wound closure is punctuated by wound edge intercalation, which can drive wound closure. **a**, Early stages of wound closure in a *sqh*^{ΔX3}; *sqh*-GFP, Ecad-tdTomato wing imaginal disc. Cell outlines are marked by Ecad-tdTomato (green) and MyoII by Sqh-GFP (magenta). Cells that will be ablated are marked by white dots at 0 min. Within the first 10 min after wounding, a strong accumulation of MyoII can be seen at the wound's edge in the manner of a purse string (arrow). Images are maximum intensity projections of deconvolved image stacks. Scale bar, 5 μm. **b**, Dynamics of wing disc wound closure. Percentage of original wound area is plotted over time for five wild-type (WT) wing discs expressing Ecad-GFP (the same five wing discs are used for all subsequent WT analyses unless otherwise stated). Inset: the first 20 min, showing early expansion (recoil) of the wound. A two-phase exponential decay curve (black line) is fitted to the data after 3 min, when the wound begins to reduce in area until closed. The transition between fast and slow closure phases of the two-phase exponential decay is marked by a dotted line (18.37 min). **c**, Quantification of MyoII purse string intensity (magenta, left y axis) and wound percentage area (green, right y axis) for three *sqh*^{ΔX3}; *sqh*-GFP, Ecad-tdTomato wing discs during the first hour of wound closure. A two-phase exponential decay curve has been fitted to the area data (green line) and a moving average (± 4 time points) curve to the MyoII intensity data (magenta line). The transition between fast and slow closure phases is shown with a dotted line (12.71 min). **d**, Example of a single wound edge intercalation in an Ecad-GFP; *sqh*-mCherry, *pnr*-GAL4 wing disc. The raw maximum intensity projection (left) and skeletonized images (right, intercalating cell in blue, wound in white) are shown. The junction shared between the intercalating cell and the wound shrinks to a point and a new junction grows in the orthogonal direction. Scale bar, 3 μm. **e**, Quantification of the percentage of starting wound edge junctions (magenta) and wound percentage area (green) for a single Ecad-GFP wing disc wound. The percentage of junctions remaining on the wound's edge reduces as intercalations occur until the wound fully closes. **f**, Quantification of intercalation rate in unwounded WT tissues and at WT wound edges. The intercalation rate is significantly higher at the wound edge (unpaired *t*-test with Welch's correction, $n = 5$, $t = 15.15$, d.f. = 5.089, $P < 0.0001$). Error bars indicate s.d. **g**, Relationship between percentage of wound start area and percentage of starting wound edge junctions remaining. The mean percentage area at which there is a transition between the fast (green) and slow (magenta) closure phases is highlighted (57.6%). A moving average curve (± 4 time points) of the data is shown. **** $P < 0.0001$.

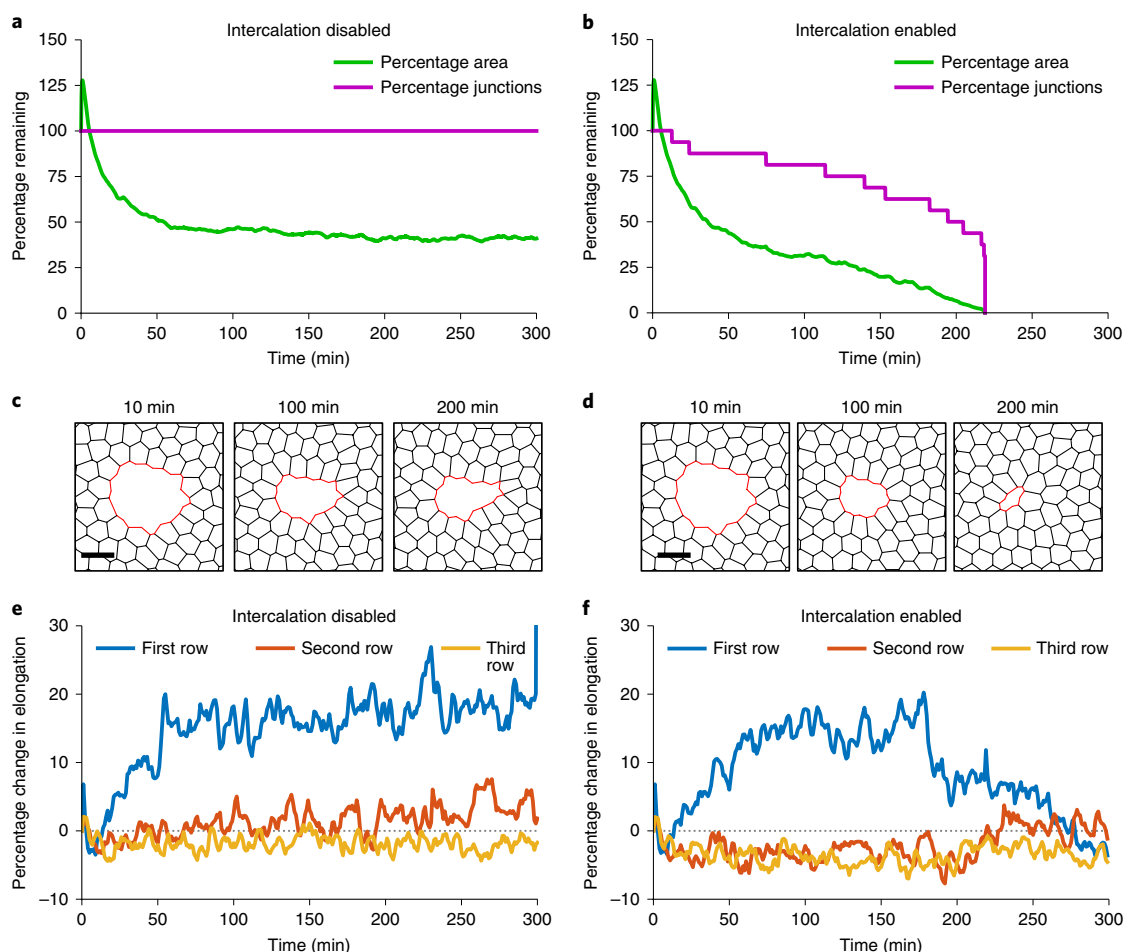


Fig. 2 | A vertex model of wound healing predicts that intercalation is necessary for wound closure and cell shape maintenance. Vertex model simulations. **a,b**, Percentage of initial wound area and wound junctions after ablation with intercalations disabled (**a**) and enabled (**b**). **c,d**, Vertex model simulation images after ablation with intercalations disabled (**c**) and enabled (**d**). Scale bar, 5 μm . **e,f**, Percentage change in cell elongation over time during and after wound closure, calculated by dividing the major axis by the minor axis of an ellipse fit to each cell, for the first three rows of cells around the wound with intercalations disabled (**e**) and enabled (**f**).

purse string, causing wound edge junctions to reduce in length. To capture experimentally observed fluctuations in junctional and purse-string MyoII²⁸, we introduced fluctuations in the line tension at cell–cell interfaces and in the purse string (Supplementary Fig. 2d). Without introducing intercalation events into the model, simulated wounds are unable to close (Fig. 2a,c and Supplementary Video 3). By contrast, when intercalations are enabled in the model (Supplementary Fig. 2c and Supplementary Methods), wounds are able to close (Fig. 2b,d and Supplementary Video 4), supporting our hypothesis that intercalations at the wound edge are necessary to drive wound closure.

The vertex model predicts that, in the absence of intercalation, cells around the wound become more elongated towards the centre of the wound (Fig. 2e) than in simulations with intercalations enabled (Fig. 2f). In both cases, the cells initially elongate as the purse string contracts the wound. As cells begin to intercalate away from the wound edge their shapes relax, reducing the elongation over time. Towards the end of wound closure, many intercalations occur (Fig. 2b), at which point the elongation rapidly decreases and the cells return to a fully relaxed state after healing (Fig. 2f). With intercalations disabled, the cells remain highly elongated (Fig. 2e). This led us to hypothesize that wound edge intercalations play a crucial role in maintaining cell shape and tissue patterning. Indeed, wing disc cells appear regularly packed immediately after wound

closure (Fig. 3a) and the polygon distribution of wound edge cells is restored upon healing (Fig. 3b). The seamless closure we observe is distinct from a number of *in vivo*^{22,29} and *in vitro*^{5,30} systems that can form visible scar-like rosette structures upon closure. To test our vertex model's prediction that intercalation preserves cell shape, we quantified cell elongation in the first three rows of cells away from the wound in wing discs (Fig. 3c and Supplementary Video 5). Although cells in the second and third rows undergo little change in elongation during wound closure (Fig. 3d), cells in the first row undergo a transient increase in elongation towards the wound (Fig. 3c–f) before returning to their original shapes prior to wound closure (Fig. 3d–f). Cells return to their original shape during the slow phase of closure (Fig. 3d,e), when the majority of intercalations occur, supporting the role of intercalation in preserving cell shape.

If intercalations are indeed required to maintain cell shape, we expect that the majority of cell intercalations should be localized to the first row of cells, as it is these cells that are being stretched (Fig. 3d). Indeed, when we quantify the intercalation rates in different rows of cells across the closure process, we find that the intercalation rate is significantly higher in the first row of cells and decays in increasing rows away from the wound edge (Fig. 3g and Supplementary Fig. 3a–c). This prediction of a localized increase in intercalation rate also holds true for our vertex model (Fig. 3g and Supplementary Fig. 3b,c). However, when the strength of the purse

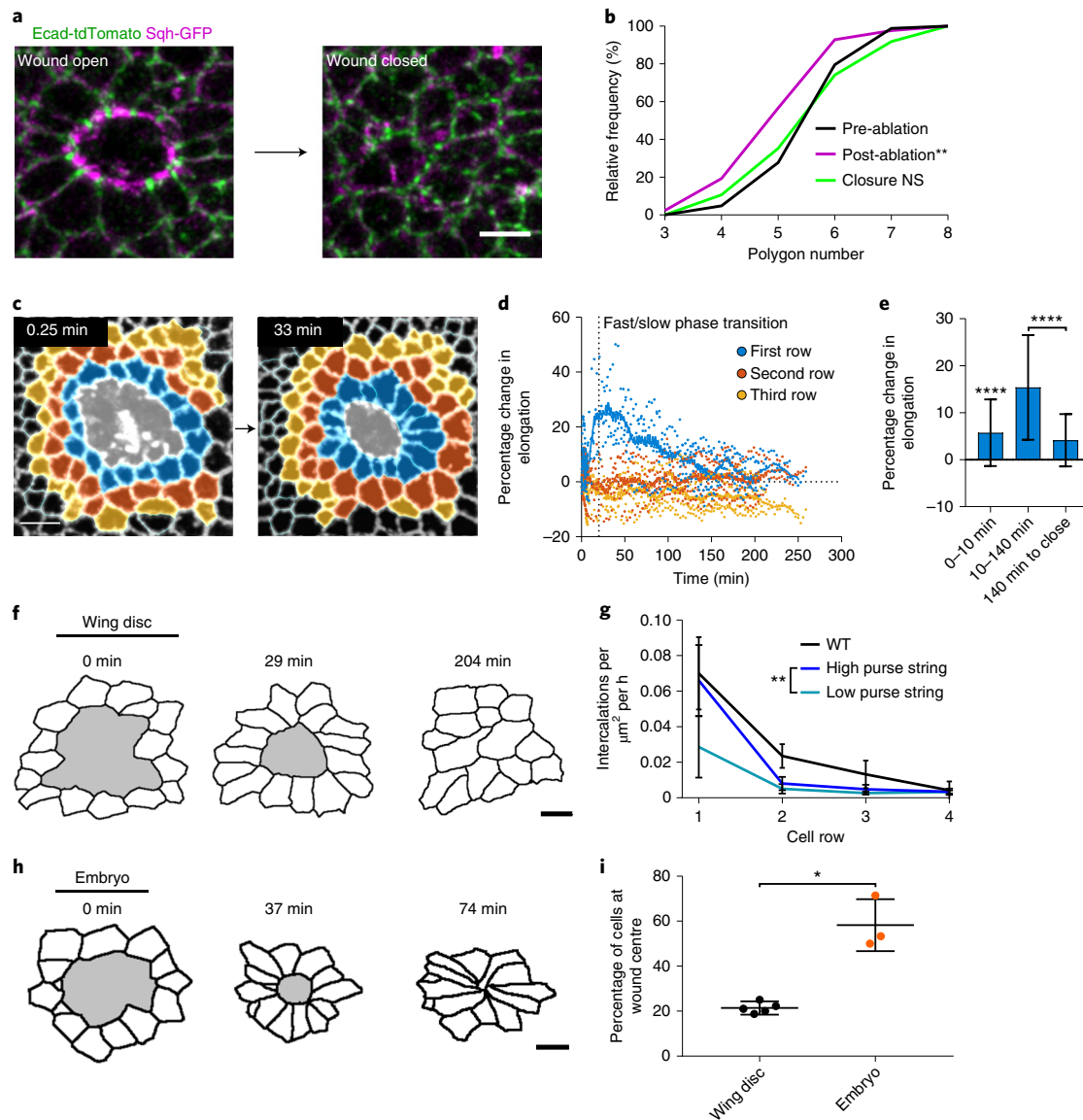


Fig. 3 | Wound edge intercalation preserves cell shape. **a**, Maximum intensity projection images of a wound in a *sqh^{AΔX3}; sqh-GFP*, *Ecad-tdTomato* wing disc before (left) and immediately after (right) wound closure. Scale bar, 3 μm . **b**, Quantification of wound edge cell polygon number before ablation, immediately after ablation and immediately after wound closure. The distribution of polygon number is significantly shifted left after ablation (Kolmogorov-Smirnov test, $D=0.2892$, $P=0.0019$) but is restored upon closure (Kolmogorov-Smirnov test, $D=0.07583$, $P=0.9692$). **c**, Colour coding of the first three rows away from the wound edge (first row, blue; second row, orange; third row, yellow) for time points immediately after wounding (0.25 min) and soon after the onset of wound edge intercalation (33 min). The images are adaptive projections of *Ecad-GFP* overlaid by skeletonized cell outlines. Scale bar, 5 μm . **d**, Quantification of the percentage change in mean cell elongation for the first three rows of cells (colour coding as in **c**) over time for five WT wounds. Moving average curves (± 4 time points) are shown. The transition between fast and slow closure phases is marked by a dotted line (18.37 min). **e**, Percentage change in mean elongation of first row cells for three time windows: 0–10 min (wound recoil), 10–140 min (early wound closure) and 140 min to close (late wound closure). Data are pooled from the dataset in **d**. Cells were significantly more elongated during the recoil phase (Wilcoxon signed rank test, $P < 0.0001$). Cells were significantly more elongated during early wound closure than during late wound closure (Kolmogorov-Smirnov test, $D=0.5703$, $P < 0.0001$). Error bars indicate s.d. **f,h**, Skeletonized cell outlines of cells starting at the wound edge (wound shaded in grey) at three time points in a single WT wing disc (scale bar, 3 μm) (**f**) and a single WT stage 13 embryo (scale bar, 5 μm) (**h**). **g**, Quantification of intercalation rates in rows of cells away from the wound for WT wing discs (black) and vertex model simulations with high (dark blue) and low (light blue) purse string strength. The intercalation rate in simulations is significantly higher in the first row of cells with a high purse string strength (Kolmogorov-Smirnov test, $D=0.6667$, $P=0.0097$). **i**, Quantification of the percentage of cells remaining close to the wound's centre after closure, as a measure of intercalation. A significantly higher percentage of cells remain close to the wound centre in embryos ($n=3$) compared with wing discs ($n=5$) (unpaired *t*-test with Welch's correction, $t=5.466$, d.f. = 2.103, $P=0.0285$). NS (not significant): $P > 0.05$, * $P < 0.05$, ** $P < 0.01$, **** $P < 0.0001$.

string is reduced, the intercalation rate in the first row of cells is significantly lower (Fig. 3g and Supplementary Fig. 3b,c). Therefore, the cell shape changes induced by the close proximity of a cell (or row of cells) to the purse string can explain the localized increase

in intercalation rate that we observe. This mechanical function of the purse string contrasts with previous work that suggests that the purse string functions mainly in setting the direction of cell movement towards the wound during wound closure⁵.

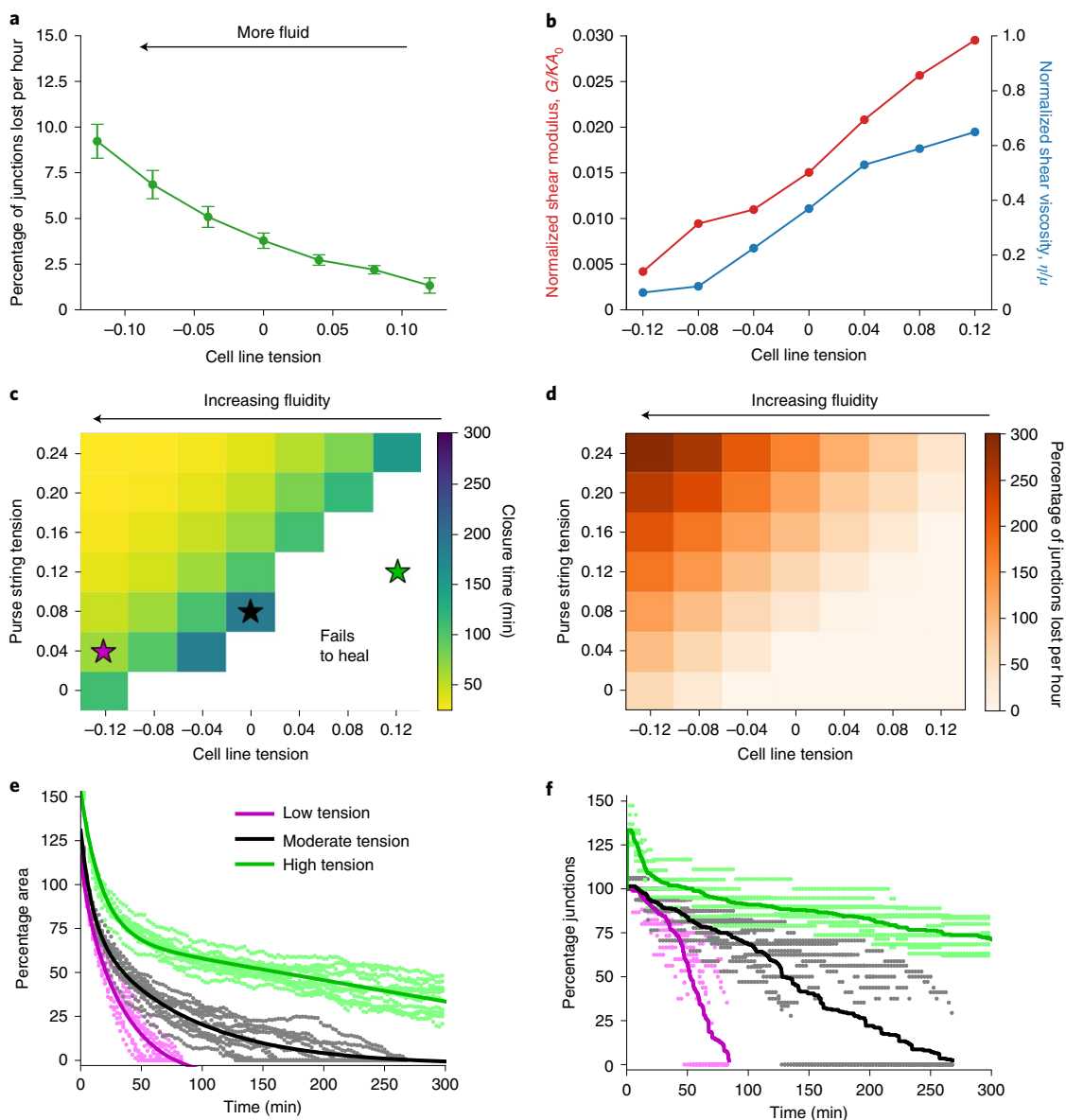


Fig. 4 | Reducing tissue contractility enhances fluidity and can speed wound closure. All panels show the results of vertex model simulations. **a**, Intercalation rate in unwounded tissue versus mean cell line tension. Error bars indicate s.d. **b**, Normalized tissue shear modulus and viscosity versus tension. **c**, Mean wound closure time versus cell line tension and purse string tension. White region, parameter space where wounds fail to close within 300 min. Coloured stars indicate the parameters used in **e** and **f**. **d**, Mean wound edge intercalation rate versus cell line tension and purse string tension. **e**, Percentage of initial area over time for low, moderate and high line tension cases. Points are from simulations and lines are dual exponential fitting curves. **f**, Percentage of initial wound junctions over time for low, moderate and high tension cases. Points are from simulations and lines are the average over all simulations. For all combinations of tension, $n = 12$ simulations for each.

Altogether, these findings suggest that intercalation events help maintain cell shape and that wound healing in an epithelium that does not intercalate will lead to cell deformation. To test this idea further, we compared wound edge intercalation in the wing disc to the *Drosophila* embryonic ectoderm, an epithelium in which cells do not return to their original shape (Fig. 3h). Following wound closure in the *Drosophila* embryonic ectoderm, cells can be up to twice as elongated as they were before wounding²². Supporting the model's predictions, there are significantly fewer wound edge intercalations in embryos before wound closure (Fig. 3i).

These results suggest that wound closure is controlled by two dynamic mechanical properties of the wounded tissue: the rate of wound edge intercalation and the tension in the purse string. We used the model to test the relative roles of intercalation rate and

purse string tension in wounded tissues. We found that the rate of intercalation in the tissue can be tuned by modulating the cell–cell interfacial tension (Fig. 4a). Similarly, the intercalation rate can also be tuned by modulating the perimeter contractility of a cell (Supplementary Fig. 4a,b). As the cell line tension decreases, the rate of intercalation in the tissue increases. This leads to an increase in ‘tissue fluidity’—the rearrangement of cells relative to each other—analogue to molecules in a liquid.

To demonstrate that a reduction in interfacial tension (increase in intercalations) indeed increases the fluidity of a tissue, we performed shear rheology simulations using our vertex model (Supplementary Fig. 5a), and computed the tissue shear modulus and viscosity with varying line tensions (Fig. 4b and Supplementary Fig. 5b–f). As the line tension is gradually reduced in simulations,

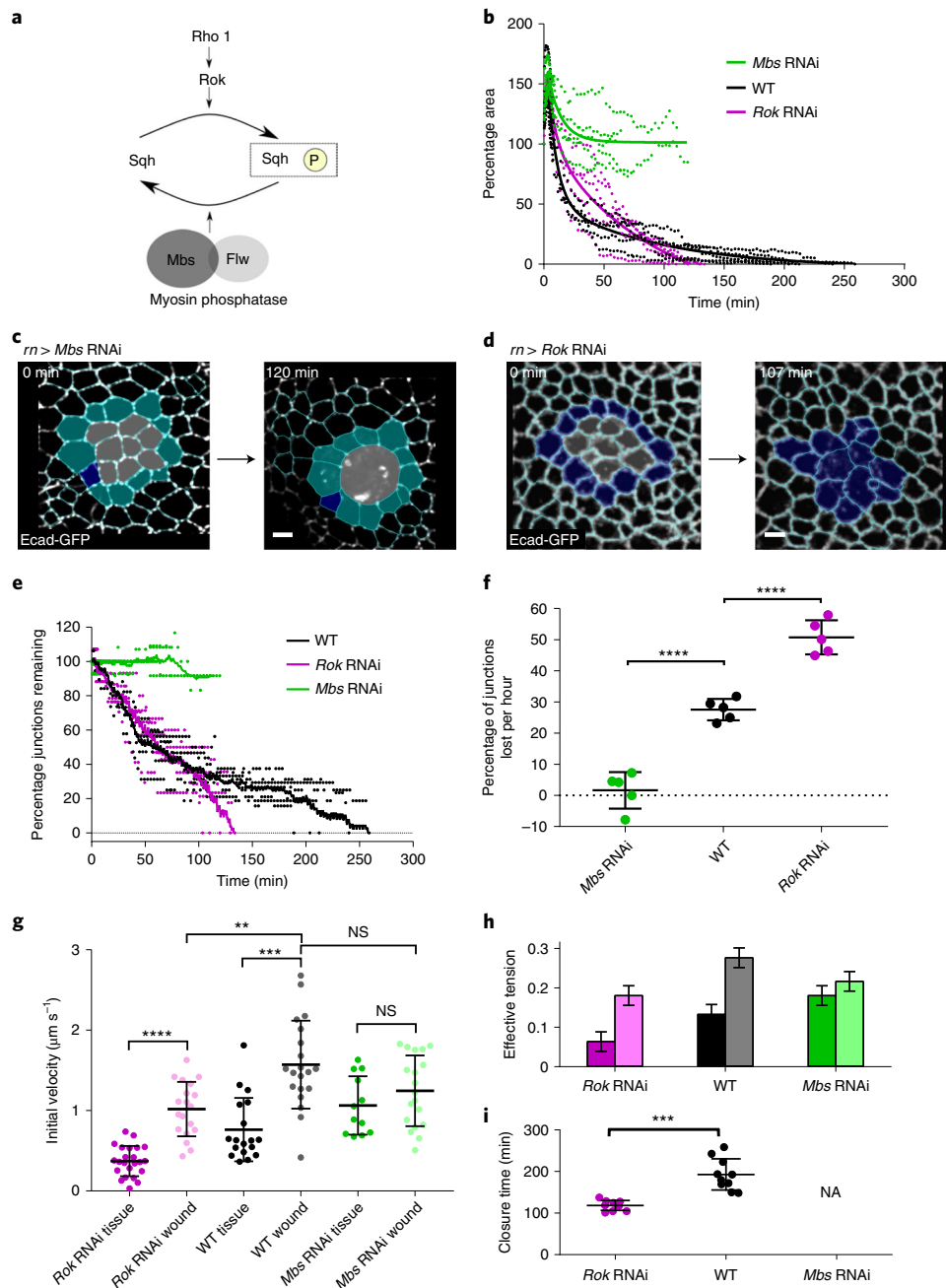


Fig. 5 | Myosin activity controls tissue fluidity and wound closure rate. **a**, Activation of MyoII by phosphorylation of its regulatory light chain (Sqh) can be performed by Rho kinase (Rok) downstream of Rho1. MyoII inactivation by Sqh dephosphorylation can be performed by the myosin phosphatase comprising the myosin binding subunit (Mbs) and catalytic subunit (Flapwing, Flw). **b**, Quantification of wound closure (as a percentage of start wound area) over time in *Mbs* RNAi (green, $n=5$) and *Rok* RNAi (magenta, $n=5$) wing discs, compared to WT wound closure (black, $n=5$). Two-phase exponential decays are fitted after 3 min. **c,d**, Examples of wound healing in *Mbs* RNAi (**c**) and *Rok* RNAi (**d**) before wounding (left) and after wound closure (right, *Rok* RNAi) or when further segmentation becomes impossible (right, *Mbs* RNAi). Cells are colour coded according to whether they undergo intercalation (dark blue) or not (cyan). Images are adaptive projections of Ecad-GFP overlaid by skeletonized cell outlines in cyan (scale bars, $3\mu\text{m}$). **e**, Quantification of the percentage of initial wound edge junctions over time for *Mbs* RNAi and *Rok* RNAi wing discs (colours and n as in **b**). Moving average curves (± 4 time points) are shown. **f**, Quantification of mean intercalation rate for *Mbs* RNAi, WT and *Rok* RNAi wounds (colours and n as in **b**). The intercalation rate is significantly higher in *Rok* RNAi wounds (unpaired t -test, $n=5$, $t=8.503$, $\text{d.f.}=8$, $P<0.0001$) and significantly lower in *Mbs* RNAi wounds (unpaired t -test, $n=5$, $t=8.503$, $\text{d.f.}=8$, $P<0.0001$) compared to WT. Error bars indicate s.d. **g**, Quantification of initial vertex recoil rates after single junction ablations in WT (black), *Mbs* RNAi (green) and *Rok* RNAi (magenta) wing discs. Junction ablations were performed in unwounded tissues ('tissue') and at wound edges ('wound'). Wound edge vertex recoil rates were significantly higher than in the surrounding tissue in WT and *Rok* RNAi discs, but not *Mbs* RNAi discs. Vertex recoil rates at the wound edge were significantly lower in *Rok* RNAi discs compared to WT discs, but were not significantly changed in *Mbs* RNAi discs. Full results of Kolmogorov-Smirnov tests are provided in Supplementary Table 1. **h**, Input mean and s.d. of effective tension (the total of line tension and contractility) for different simulated conditions. Left bars, bulk edges; right bars, wound edges. **i**, Mean wound closure time for the simulated conditions. *Mbs* RNAi simulated wounds fail to heal. NA, not applicable. Error bars indicate s.d. Wound closure time is significantly lower in *Rok* RNAi wounds than WT wounds (unpaired t -test, $n=10$, $t=6.298$, $\text{d.f.}=18$, $P<0.0001$). NS: $P>0.05$, *** $P<0.001$, **** $P<0.0001$.

both the shear modulus and viscosity approach zero³¹. Our findings stand in contrast to previous studies, which suggested that cell monolayers displaying viscous-like behaviours with many cell rearrangements³² fail to close wounds⁶. However, our results are consistent with the suggestion that increasing monolayer elasticity would prevent wound closure².

Simulations using our vertex model also demonstrate that the intercalation rate can increase rapidly when the magnitude of line tension fluctuations is increased (Supplementary Fig. 4d), leading to a smaller corresponding reduction in closure time (Supplementary Fig. 4c). However, when the tension fluctuations are large, the intercalation rate in unwounded simulations far exceeds what we observe in unwounded tissues (Fig. 1f) with many short-timescale reversible intercalations. We do not observe large numbers of reversible intercalations in the wing disc, so it is unlikely that higher tension fluctuations are physiologically relevant. Simulations also demonstrate that cell division rates can affect closure time (Supplementary Fig. 4e). However, the range of cell division rates used in these simulations far exceeds the physiological range of cell division rates we have measured in a number of genetic conditions (Supplementary Fig. 4e). Accordingly, it is unlikely that cell division has a strong contribution to wing disc wound closure for wounds of this size, unlike for larger wounds³³. Although varying the magnitude of tension fluctuations and divisions rates is not physiologically relevant, the observation that both can be modulated to increase fluidity, and subsequently wound closure rate (Supplementary Fig. 4c–f), demonstrates that fluidity-driven wound closure is likely to be a general phenomenon.

Either increasing the purse string tension or decreasing the cell line tension reduces the time taken for wounds to close (Fig. 4c) and increases the rate of wound edge intercalations (Fig. 4d). Unexpectedly, we find a region of parameter space where a reduction in purse string tension is more than compensated by an increase in tissue fluidity (decrease in tension), leading to accelerated wound closure (Fig. 4c,e,f, magenta compared to black). However, tissue fluidity can only rescue a reduced purse string up to a point, as the majority of simulations with the weakest purse string tension values fail to close, regardless of the level of tissue fluidity (Fig. 4c,e,f). This observation highlights the importance of the purse string for the increase in wound edge intercalation (Fig. 3g and Supplementary Fig. 3). Together, these results demonstrate that bulk tissue mechanical properties and the activity of the purse string cooperate to promote wound closure.

To test these predictions from our vertex model further, we sought to experimentally perturb the cell edge tension. In epithelial tissues, cell edge tension is governed by the activity of non-muscle MyoII (Fig. 5a). To test the roles of purse string tension and tissue fluidity in the wing disc, we genetically modulated the activity of MyoII in the wing pouch epithelium. To increase the tension, we performed RNA interference (RNAi) against the myosin binding subunit (*Mbs*) of myosin phosphatase, a phosphatase that inactivates MyoII by dephosphorylating its regulatory light chain³⁴ (Spaghetti squash (*Sqh*) in *Drosophila*). To decrease the tension, we performed RNAi against rho-kinase (*Rok*), a kinase that activates MyoII by phosphorylating *Sqh*^{35,36}. We confirmed the effect of these genetic perturbations on tension by quantifying the vertex recoil rates (a greater recoil rate implying higher tension) after single junction ablations in unwounded tissues (Fig. 5g). We then wounded these wing discs and compared the dynamics of wound closure to that in WT wing discs (Supplementary Fig. 6a–d). In *Mbs* RNAi wing discs, where tension is high, wounds fail to close within the imaging time window (Fig. 5b,c, Supplementary Figs. 6a and 7 and Supplementary Video 6). Furthermore, wound edge cell intercalation is almost entirely abolished (Fig. 5c,e,f, Supplementary Fig. 7 and Supplementary Video 6), supporting the importance of intercalation in promoting wound closure.

In *Rok* RNAi wing discs (Supplementary Fig. 8 and Supplementary Video 7), in which tension is reduced, wounds close faster than in WT wing discs. Although these wounds initially close more slowly than WT wounds, they eventually overtake them and unexpectedly close in roughly half the time of WT wounds (Fig. 5b,d and Supplementary Fig. 6a). This is accompanied by an increase in the rate of wound edge intercalation (Fig. 5d–f). A decrease in interfacial tension can also be achieved via an increase in cell–cell adhesion. An increase in cell–cell adhesion is thought to promote cell–cell contact formation, effectively counteracting junction contractility³⁷. In line with this prediction, we obtained intercalation and closure rates similar to *Rok* RNAi wing discs when we expressed double the number of copies of the adherens junction-associated cell–cell adhesion molecule E-cadherin (ubi-Ecad-GFP; Supplementary Figs. 6a–d and 9a–h). Therefore, decreased interfacial tension appears to be a general route to increasing tissue fluidity and wound closure rate, regardless of the origin of the tension decrease.

One consequence of decreasing MyoII activity through *Rok* RNAi, is that it is likely to increase tissue fluidity, while simultaneously decreasing purse string tension^{8,38}. To quantify the effects of MyoII perturbations on tension in the surrounding tissue and in the purse string, we ablated single junctions at the wound edge and in the surrounding tissue in all three conditions and compared the initial vertex recoil velocities that serve as a measure of junctional tension³⁹ (Fig. 5g and Supplementary Table 1). In WT tissues, the junction recoil rate in the purse string is twice that of the surrounding tissue. This mimics the relative increase in MyoII intensity we observed in WT wing discs (Fig. 1c). In *Rok* RNAi wing discs, vertex recoil rates are reduced by 51% in the tissue and 35% in the purse string compared to WT. One would therefore predict that the increase in tissue fluidity in *Rok* RNAi discs, associated with a large decrease in tension in the surrounding tissue, may be able to more than compensate for the reduction in purse string strength, as predicted by our model (Fig. 4c). In *Mbs* RNAi wing discs, vertex recoil rates are increased by 40% in the tissue and decreased by 21% in the purse string compared to WT. The decrease in both tissue fluidity (due to increased tissue junctional tension) and purse string strength probably explains why wounds in *Mbs* RNAi discs fail to close. Interestingly, *Mbs* RNAi purse string vertex recoil rates are not significantly higher than vertex recoil rates in either the WT purse string or *Mbs* RNAi tissue (Fig. 5g and Supplementary Table 1). This suggests that we have elevated tension in the wing disc to its maximum possible level through *Mbs* RNAi, a level that is also achieved in the purse string of WT discs. To test whether the measured vertex recoil rates in the three experimental conditions can predict wound closure rates, we used the measured vertex recoil rates as an input to our model by assuming that the total edge tension is proportional to the recoil rate (Fig. 5h and Supplementary Methods). We also used experimentally measured division rates for WT, *Rok* RNAi and *Mbs* RNAi (Supplementary Fig. 4e), although these rates show little variation and cannot explain the changes in wound closure rate. We find that the differences in the experimentally measured tensions are sufficient to explain the increased healing rate in *Rok* RNAi and failed healing in *Mbs* RNAi (Fig. 5i).

We have thus demonstrated that wing disc wound closure is dependent on cell–cell intercalation-driven tissue fluidity, downstream of interfacial junctional tension. The dynamics of wound closure in wing discs can be explained purely through junctional behaviours in our vertex model, rather than previously described cell-crawling based migration^{30,40–42}. In our system, fluidity may substitute for the propulsive action provided by cell crawling, as it provides a mechanism for energy dissipation, which leads to mechanical relaxation²⁷ (Supplementary Fig. 10a–c). The dispensability of crawling for our system is reminiscent of the closure of cell monolayer wounds over non-adherent environments^{3,6}, which entirely depends on purse string tensile activity. In these studies,

wounds close much more slowly than in wing discs and a reinforcement of purse string strength is thought to be required for closure⁶. Both these differences may be explained by a failure of these monolayers to efficiently dissipate energy, unlike in wing discs (Supplementary Fig. 10a–c).

Changes in tension-based fluidity, such as those we have induced through MyoII perturbation, can be interpreted as an unjamming transition^{43,44}. Epithelial tissues can transition between a fluid-like state (unjammed) with many rearrangements and a solid-like jammed state, lacking the ability to rearrange^{43–45}. Theoretical models have described how jamming/unjamming transitions can be induced via changes in junctional tension and cell–cell adhesion⁴⁶. These two properties define a mechanical energy barrier, which must be overcome for cells to rearrange relative to each other^{43,46}, allowing an epithelium to behave as a fluid. By reducing tension in the wing disc, we are probably lowering this energy barrier, allowing cells to rearrange more. Simulations indeed demonstrate that, with increased intercalations, tissues can transit to a lower energy state during wound healing, which may allow further intercalations to occur (Supplementary Fig. 10a–c). The role we describe for tissue fluidity in wound healing, in addition to its known roles in developing^{28,47–50} and mature tissues⁴⁶, reinforces the physiological importance of the fluid state of a tissue.

Reporting Summary. Further information on research design is available in the Nature Research Reporting Summary linked to this Article.

Online content

Any methods, additional references, Nature Research reporting summaries, source data, statements of code and data availability and associated accession codes are available at <https://doi.org/10.1038/s41567-019-0618-1>.

Data availability

The data that support the findings of this study are available from the corresponding author upon reasonable request.

Code availability

The code that supports the findings of this study are available from the corresponding author upon reasonable request.

Received: 6 August 2018; Accepted: 1 July 2019;

Published online: 12 August 2019

References

- Ladoux, B. & Mege, R. M. Mechanobiology of collective cell behaviours. *Nat. Rev. Mol. Cell Biol.* **18**, 743–757 (2017).
- Cochet-Escartin, O., Ranft, J., Silberzan, P. & Marcq, P. Border forces and friction control epithelial closure dynamics. *Biophys. J.* **106**, 65–73 (2014).
- Nier, V. et al. Tissue fusion over nonadhering surfaces. *Proc. Natl Acad. Sci. USA* **112**, 9546–9551 (2015).
- Arciero, J. C., Mi, Q., Branca, M. F., Hackam, D. J. & Swigon, D. Continuum model of collective cell migration in wound healing and colony expansion. *Biophys. J.* **100**, 535–543 (2011).
- Brugues, A. et al. Forces driving epithelial wound healing. *Nat. Phys.* **10**, 683–690 (2014).
- Vedula, S. R. K. et al. Mechanics of epithelial closure over non-adherent environments. *Nat. Commun.* **6**, 6111 (2015).
- Begnaud, S., Chen, T. C., Delacour, D., Mege, R. M. & Ladoux, B. Mechanics of epithelial tissues during gap closure. *Curr. Opin. Cell Biol.* **42**, 52–62 (2016).
- Russo, J. M. et al. Distinct temporal-spatial roles for Rho kinase and myosin light chain kinase in epithelial purse-string wound closure. *Gastroenterology* **128**, 987–1001 (2005).
- Abreu-Blanco, M. T., Verboon, J. M., Liu, R., Watts, J. J. & Parkhurst, S. M. *Drosophila* embryos close epithelial wounds using a combination of cellular protrusions and an actomyosin purse string. *J. Cell Sci.* **125**, 5984–5997 (2012).
- Wood, W. et al. Wound healing recapitulates morphogenesis in *Drosophila* embryos. *Nat. Cell Biol.* **4**, 907–912 (2002).
- Brock, J., Midwinter, K., Lewis, J. & Martin, P. Healing of incisional wounds in the embryonic chick wing bud: characterization of the actin purse-string and demonstration of a requirement for Rho activation. *J. Cell Biol.* **135**, 1097–1107 (1996).
- Davidson, L. A., Ezin, A. M. & Keller, R. Embryonic wound healing by apical contraction and ingression in *Xenopus laevis*. *Cell Motil. Cytoskeleton* **53**, 163–176 (2002).
- Zulueta-Coarasa, T. & Fernandez-Gonzalez, R. Dynamic force patterns promote collective cell movements during embryonic wound repair. *Nat. Phys.* **14**, 750–758 (2018).
- Kobb, A. B., Zulueta-Coarasa, T. & Fernandez-Gonzalez, R. Tension regulates myosin dynamics during *Drosophila* embryonic wound repair. *J. Cell Sci.* **130**, 689–696 (2017).
- Bement, W. M., Forscher, P. & Mooseker, M. S. A novel cytoskeletal structure involved in purse string wound closure and cell polarity maintenance. *J. Cell Biol.* **121**, 565–578 (1993).
- Martin, P. & Lewis, J. Actin Cables and epidermal movement in embryonic wound-healing. *Nature* **360**, 179–183 (1992).
- Bement, W. M., Mandato, C. A. & Kirsch, M. N. Wound-induced assembly and closure of an actomyosin purse string in *Xenopus* oocytes. *Curr. Biol.* **9**, 579–587 (1999).
- Danjo, Y. & Gipsen, I. K. Actin ‘purse string’ filaments are anchored by E-cadherin-mediated adherens junctions at the leading edge of the epithelial wound, providing coordinated cell movement. *J. Cell Sci.* **111**, 3323–3332 (1998).
- Heller, D. et al. EpiTools: an open-source image analysis toolkit for quantifying epithelial growth dynamics. *Dev. Cell* **36**, 103–116 (2016).
- Galko, M. J. & Krasnow, M. A. Cellular and genetic analysis of wound healing in *Drosophila* larvae. *PLoS Biol.* **2**, 1114–1126 (2004).
- Losick, V. P., Fox, D. T. & Spradling, A. C. Polyploidization and cell fusion contribute to wound healing in the adult *Drosophila* epithelium. *Curr. Biol.* **23**, 2224–2232 (2013).
- Razzell, W., Wood, W. & Martin, P. Recapitulation of morphogenetic cell shape changes enables wound re-epithelialisation. *Development* **141**, 1814–1820 (2014).
- Tetley, R. J. & Mao, Y. The same but different: cell intercalation as a driver of tissue deformation and fluidity. *Phil. Trans. R. Soc. Lond. B Biol. Sci.* **373**, 20170328 (2018).
- Fletcher, A. G., Osterfield, M., Baker, R. E. & Shvartsman, S. Y. Vertex models of epithelial morphogenesis. *Biophys. J.* **106**, 2291–2304 (2014).
- Wyczalkowski, M. A., Varner, V. D. & Taber, L. A. Computational and experimental study of the mechanics of embryonic wound healing. *J. Mech. Behav. Biomed.* **28**, 125–146 (2013).
- Barton, D. L., Henkes, S., Weijer, C. J. & Sknepnek, R. Active vertex model for cell-resolution description of epithelial tissue mechanics. *PLoS Comput. Biol.* **13**, e1005569 (2017).
- Staddon, M. F. et al. Cooperation of dual modes of cell motility promotes epithelial stress relaxation to accelerate wound healing. *PLoS Comput. Biol.* **14**, e1006502 (2018).
- Curran, S. et al. Myosin II controls junction fluctuations to guide epithelial tissue ordering. *Dev. Cell* **43**, 480–492 (2017).
- Shindo, A. et al. Septin-dependent remodeling of cortical microtubule drives cell reshaping during epithelial wound healing. *J. Cell Sci.* **131**, 212647 (2018).
- Anon, E. et al. Cell crawling mediates collective cell migration to close undamaged epithelial gaps. *Proc. Natl Acad. Sci. USA* **109**, 10891–10896 (2012).
- Bi, D. P., Lopez, J. H., Schwarz, J. M. & Manning, M. L. A density-independent rigidity transition in biological tissues. *Nat. Phys.* **11**, 1074–1079 (2015).
- Vedula, S. R. et al. Epithelial bridges maintain tissue integrity during collective cell migration. *Nat. Mater.* **13**, 87–96 (2014).
- Bergantinos, C., Corominas, M. & Serras, F. Cell death-induced regeneration in wing imaginal discs requires JNK signalling. *Development* **137**, 1169–1179 (2010).
- Vereshchagina, N. et al. The essential role of PP1 beta in *Drosophila* is to regulate nonmuscle myosin. *Mol. Biol. Cell* **15**, 4395–4405 (2004).
- Amano, M. et al. Phosphorylation and activation of myosin by Rho-associated kinase (Rho-kinase). *J. Biol. Chem.* **271**, 20246–20249 (1996).
- Mizuno, T., Amano, M., Kaibuchi, K. & Nishida, Y. Identification and characterization of *Drosophila* homolog of Rho-kinase. *Gene* **238**, 437–444 (1999).
- Lecuit, T. & Lenne, P. F. Cell surface mechanics and the control of cell shape, tissue patterns and morphogenesis. *Nat. Rev. Mol. Cell Biol.* **8**, 633–644 (2007).
- Verboon, J. M. & Parkhurst, S. M. Rho family GTPase functions in *Drosophila* epithelial wound repair. *Small GTPases* **6**, 28–35 (2015).
- Farhadifar, R., Roper, J. C., Algouy, B., Eaton, S. & Julicher, F. The influence of cell mechanics, cell–cell interactions, and proliferation on epithelial packing. *Curr. Biol.* **17**, 2095–2104 (2007).

40. Chepizhko, O. et al. From jamming to collective cell migration through a boundary induced transition. *Soft Matter* **14**, 3774–3782 (2018).
41. Brugués, A. et al. Forces driving epithelial wound healing. *Nat. Phys.* **10**, 684–691 (2014).
42. Fenteany, G., Janmey, P. A. & Stossel, T. P. Signaling pathways and cell mechanics involved in wound closure by epithelial cell sheets. *Curr. Biol.* **10**, 831–838 (2000).
43. Park, J. A., Atia, L., Mitchel, J. A., Fredberg, J. J. & Butler, J. P. Collective migration and cell jamming in asthma, cancer and development. *J. Cell Sci.* **129**, 3375–3383 (2016).
44. Sadati, M., Qazvini, N. T., Krishnan, R., Park, C. Y. & Fredberg, J. J. Collective migration and cell jamming. *Differentiation* **86**, 121–125 (2013).
45. Liu, A. J. & Nagel, S. R. Nonlinear dynamics—jamming is not just cool any more. *Nature* **396**, 21–22 (1998).
46. Park, J. A. et al. Unjamming and cell shape in the asthmatic airway epithelium. *Nat. Mater.* **14**, 1040–1048 (2015).
47. Miroshnikova, Y. A. et al. Adhesion forces and cortical tension couple cell proliferation and differentiation to drive epidermal stratification. *Nat. Cell Biol.* **20**, 69–80 (2018).
48. Firmino, J., Rocancourt, D., Saadaoui, M., Moreau, C. & Gros, J. Cell division drives epithelial cell rearrangements during gastrulation in chick. *Dev. Cell* **36**, 249–261 (2016).
49. Petridou, N. I., Grigolon, S., Salbreux, G., Hannezo, E. & Heisenberg, C. P. Fluidization-mediated tissue spreading by mitotic cell rounding and non-canonical Wnt signalling. *Nat. Cell Biol.* **21**, 169–178 (2019).
50. Mongera, A. et al. A fluid-to-solid jamming transition underlies vertebrate body axis elongation. *Nature* **561**, 401–405 (2018).

Acknowledgements

R.J.T. was funded by a Medical Research Council Skills Development Fellowship (MR/N014529/1). M.F.S. is supported by an EPSRC funded PhD Studentship at the UCL Department of Physics and Astronomy. D.H. was supported by the Swiss National

Science Foundation (31003A-160095). S.B. acknowledges support from Royal Society University Research Fellowship (URF/R1/180187), and a Strategic Fellowship from the UCL Institute for the Physics of Living Systems. Y.M. is funded by a Medical Research Council Fellowship (MR/L009056/1), a UCL Excellence Fellowship, a NSFC International Young Scientist Fellowship (31650110472) and a Lister Institute Research Prize Fellowship. This work was also supported by MRC funding to the MRC LMxCB University Unit at UCL (award code MC_U12266B). We thank all members of the Mao group, M. Raff, D. Ish-Horowicz and M. Murrell for providing feedback on the manuscript. We also thank the Baum and Tapon laboratories for sharing fly stocks.

Author contributions

R.J.T. and Y.M. conceived the experiments. S.B. and M.F.S. conceived the theory. R.J.T. performed the experiments and analysed the data. M.F.S. ran simulations and analysed the data. D.H. and A.H. developed new image analysis tools in EpiTools and wrote the corresponding methods. R.J.T., M.F.S., S.B. and Y.M. wrote the manuscript.

Competing interests

The authors declare no competing interests.

Additional information

Supplementary information is available for this paper at <https://doi.org/10.1038/s41567-019-0618-1>.

Reprints and permissions information is available at www.nature.com/reprints.

Correspondence and requests for materials should be addressed to Y.M.

Peer review information: *Nature Physics* thanks Marino Arroyo and the other, anonymous, reviewer(s) for their contribution to the peer review of this work.

Publisher's note: Springer Nature remains neutral with regard to jurisdictional claims in published maps and institutional affiliations.

© The Author(s), under exclusive licence to Springer Nature Limited 2019

Reporting Summary

Nature Research wishes to improve the reproducibility of the work that we publish. This form provides structure for consistency and transparency in reporting. For further information on Nature Research policies, see [Authors & Referees](#) and the [Editorial Policy Checklist](#).

Statistical parameters

When statistical analyses are reported, confirm that the following items are present in the relevant location (e.g. figure legend, table legend, main text, or Methods section).

n/a | Confirmed

- The exact sample size (n) for each experimental group/condition, given as a discrete number and unit of measurement
- An indication of whether measurements were taken from distinct samples or whether the same sample was measured repeatedly
- The statistical test(s) used AND whether they are one- or two-sided
Only common tests should be described solely by name; describe more complex techniques in the Methods section.
- A description of all covariates tested
- A description of any assumptions or corrections, such as tests of normality and adjustment for multiple comparisons
- A full description of the statistics including central tendency (e.g. means) or other basic estimates (e.g. regression coefficient) AND variation (e.g. standard deviation) or associated estimates of uncertainty (e.g. confidence intervals)
- For null hypothesis testing, the test statistic (e.g. F , t , r) with confidence intervals, effect sizes, degrees of freedom and P value noted
Give P values as exact values whenever suitable.
- For Bayesian analysis, information on the choice of priors and Markov chain Monte Carlo settings
- For hierarchical and complex designs, identification of the appropriate level for tests and full reporting of outcomes
- Estimates of effect sizes (e.g. Cohen's d , Pearson's r), indicating how they were calculated
- Clearly defined error bars
State explicitly what error bars represent (e.g. SD, SE, CI)

Our web collection on [statistics for biologists](#) may be useful.

Software and code

Policy information about [availability of computer code](#)

Data collection Zen (14.0.4.201), Surface Evolver (2.70)

Data analysis Epitools (2.1.6), Fiji (1.52e), R Studio (1.0.136), Prism (7.02), Python (3.5)

For manuscripts utilizing custom algorithms or software that are central to the research but not yet described in published literature, software must be made available to editors/reviewers upon request. We strongly encourage code deposition in a community repository (e.g. GitHub). See the Nature Research [guidelines for submitting code & software](#) for further information.

Data

Policy information about [availability of data](#)

All manuscripts must include a [data availability statement](#). This statement should provide the following information, where applicable:

- Accession codes, unique identifiers, or web links for publicly available datasets
- A list of figures that have associated raw data
- A description of any restrictions on data availability

The data that support the findings of this study are available from the corresponding author upon reasonable request.

Field-specific reporting

Please select the best fit for your research. If you are not sure, read the appropriate sections before making your selection.

Life sciences Behavioural & social sciences Ecological, evolutionary & environmental sciences

For a reference copy of the document with all sections, see [nature.com/authors/policies/ReportingSummary-flat.pdf](https://www.nature.com/authors/policies/ReportingSummary-flat.pdf)

Life sciences study design

All studies must disclose on these points even when the disclosure is negative.

Sample size	See Methods, Statistical Information
Data exclusions	No data was excluded from the analyses.
Replication	See Methods, Statistical Information
Randomization	Samples were allocated to groups by genotype. Individual larvae were selected at random.
Blinding	Blinding was not possible due to clearly visible differences in phenotype between genetic conditions.

Reporting for specific materials, systems and methods

Materials & experimental systems

n/a	Involvement in the study
<input checked="" type="checkbox"/>	<input type="checkbox"/> Unique biological materials
<input checked="" type="checkbox"/>	<input type="checkbox"/> Antibodies
<input checked="" type="checkbox"/>	<input type="checkbox"/> Eukaryotic cell lines
<input checked="" type="checkbox"/>	<input type="checkbox"/> Palaeontology
<input type="checkbox"/>	<input checked="" type="checkbox"/> Animals and other organisms
<input checked="" type="checkbox"/>	<input type="checkbox"/> Human research participants

Methods

n/a	Involvement in the study
<input checked="" type="checkbox"/>	<input type="checkbox"/> ChIP-seq
<input checked="" type="checkbox"/>	<input type="checkbox"/> Flow cytometry
<input checked="" type="checkbox"/>	<input type="checkbox"/> MRI-based neuroimaging

Animals and other organisms

Policy information about [studies involving animals](#); [ARRIVE guidelines](#) recommended for reporting animal research

Laboratory animals	Drosophila melanogaster, which have no licensing restrictions.
Wild animals	The study did not involve wild animals.
Field-collected samples	The study did not involve samples collected from the field.